Preparatory Slip in Laboratory Faults: Effects of Roughness and Loading Rate

Simon Guérin-Marthe[1], Grzegorz Kwiatek[2], Lei Wang[3], Audrey Bonnelye[4], Patricia Martínez-Garzón[5], and Georg Dresen[6]

[1]Helmholtz Centre Potsdam, GFZ German Research Centre for Geosciences,
[2]Helmholtz Centre Potsdam GFZ German Research Centre for Geosciences
[3]Helmholtz-Zentrum Potsdam - Deutsches Geoforschungszentrum
[4]GFZ
[5]Helmholtz Centre Potsdam GFZ German Research for Geosciences
[6]GFZ Potsdam

November 24, 2022

Abstract

Aseismic slip may occur during a long preparatory phase preceding earthquakes, and what controls it remains poorly understood. In this study, we explored the potential dependencies of the slow slip during the preparatory stage prior to stick-slip instabilities on two main factors, namely the loading rate and surface roughness. To that end, we conducted shear stress-driven friction experiments by imposing varying loading rates on sawcut granite samples with different surface roughness at confining pressure of 35 MPa. We measured the average slip along the fault using far-field displacements and strain changes, while using acoustic emission sensors and local strain gages to capture local slip variations. We found that the average aseismic slip during preparatory stage increases with roughness, whereas its duration decreases with increased loading rate. These results also evidence a complex slip pattern on rough faults which leads to dynamic ruptures at high loading rates.

Preparatory Slip in Laboratory Faults:
Effects of Roughness and Loading Rate

Simon Guérin-Marthe[1], Grzegorz Kwiatek[1], Lei Wang[1], Audrey Bonnelye[1,2], Patricia Martínez-Garzón[1], Georg Dresen[1,3]

[1]Helmholtz Centre Potsdam, GFZ German Research Centre for Geosciences, Section 4.2: Geomechanics and Scientific Drilling, Potsdam, Germany.
[2]Free University Berlin, Berlin, Germany
[3]University of Potsdam, Potsdam, Germany

Corresponding author: Simon Guérin-Marthe (simongm@gfz-potsdam.de)

Key Points:

- The spatio-temporal slip distribution during the preparatory phase of stick-slips differs between rough and smooth faults.
- The average amount of preparatory slip increases with roughness and the duration of the preparatory phase decreases with increasing loading rate.
- Smooth faults are more prone to instability than rough faults, and increasing loading rate on rough faults promotes instability.

Abstract

Aseismic slip may occur during a long preparatory phase preceding earthquakes, and what controls it remains poorly understood. In this study, we explored the potential dependencies of the slow slip during the preparatory stage prior to stick-slip instabilities on two main factors, namely the loading rate and surface roughness. To that end, we conducted shear stress-driven friction experiments by imposing varying loading rates on sawcut granite samples with different surface roughness at confining pressure of 35 MPa. We measured the average slip along the fault using far-field displacements and strain changes, while using acoustic emission sensors and local strain gages to capture local slip variations. We found that the average aseismic slip during preparatory stage increases with roughness, whereas its duration decreases with increased loading rate. These results also evidence a complex slip pattern on rough faults which leads to dynamic ruptures at high loading rates.

Plain Language Summary

Earthquakes occur mostly along preexisting faults in the earth crust. These faults exhibit various geometrical complexities and are subjected to different strain rates. In the laboratory, we produce earthquake analogues by sliding sawcut granite blocks. We vary the geometrical complexity of the faults by roughening their surfaces and modify the strain rate by displacing the blocks at varying velocities. Under these different conditions, we measure how the forces accumulated by friction are released, by measuring stresses and displacements applied on the block's edges, using local strain deformation sensors, and by recording very small earthquakes occurring during sliding along the sawcut faults. We find that smooth sawcut faults tend to release all the energy accumulated very abruptly, after a very small amount of slip, regardless of the loading rate applied. The processes leading to failure in the case of a rough fault are much more complex, involving a large amount of slip, and numerous small earthquakes which are distributed heterogeneously in space and time.

1 Introduction

A preparation phase preceding dynamic ruptures has been observed for a large number of natural earthquakes (Bouchon et al., 2013; Durand et al., 2020; A. Kato et al., 2012; Ruiz et al., 2014), and prior dynamic ruptures in the laboratory (Dresen et al., 2020; Yamashita et al., 2021). At a shorter time scale, a nucleation phase can also be observed both in the field (Tape et al., 2018) and in the laboratory (Latour et al., 2013). Nucleation involves accelerated slip over a finite patch beyond peak stress at the rupture front (Latour et al., 2013; Rice, 1983). Previous laboratory studies have revealed that the preparatory and nucleation phase prior to dynamic instability can be explained by some combination of the 'cascade' and the 'preslip' models (Ellsworth & Beroza, 1995, McLaskey, 2019). Once a fault is close to failure, multiscale observations suggest that loading of asperities due to aseismic preslip and by stress transfer between foreshocks may occur concurrently (Kato & Ben-Zion, 2021; McLaskey, 2019; Yamashita et al., 2021). However, how preparatory and nucleation phases are linked and what controls the spatio-temporal distribution of slip during run-up to failure is still poorly understood. In addition, it remains debated in which cases this preparatory phase leads to commonly observed stick-slip instabilities in the laboratory where a dynamic rupture front passes through the whole contact interface.

Several factors have been proposed to influence the preparatory phase and the failure mode of a fault, including roughness (Harbord et al., 2017; Morad et al., 2022; Okubo & Dieterich, 1984), loading rate (Guérin-Marthe et al., 2019; Kato et al., 1992; Marone, 1998; Mclaskey & Yamashita, 2017), injection rate for permeable faults (Wang et al., 2020), (effective) normal stress state (Latour et al., 2013; Passelègue et al., 2020) and healing time (Marone, 1998). Looking at these controlling parameters individually reveals a complex picture. Morad et al. (2022) argued that an optimal roughness for triggering stick-slip instabilities on sawcut faults may exist, and Harbord et al., (2017) experimentally suggested that fault stability in granite is governed by a combination of roughness and normal stress almost irrespective of velocity strengthening and weakening behavior. Earlier work from Ohnaka (1973) already showed that for a given roughness, slip stability depends on the hardness of the two fault blocks in contact. Zhuo et al. (2022) highlighted controversial findings concerning the effect of loading rate on slip. In cases, enhanced loading rates were observed to promote instabilities (Guérin-Marthe et al., 2019; Kato et al., 1992; McLaskey & Yamashita, 2017), while other studies suggested the opposite (Karner & Marone, 2000; Ohnaka, 1973). However, cumulative slip (Zhuo et al., 2022), healing times and hold periods in slide-hold-slide tests (Guerin-Marthe, 2019) varied between these studies possibly affecting slip.

In our study, we investigate the combined influence of roughness and loading rate on the stability and preparatory phase of laboratory stick-slip events in granite sawcut samples under triaxial stress conditions. In particular, we focus on the spatio-temporal distribution of slip prior and during instabilities using far-field mechanical data, local strain gage sensors and a dense network of piezoelectric transducers.

2 Materials and Methods

Three cylindrical samples were prepared from La Peyratte granite with dimensions of 100 mm in length and 50 mm in diameter (Young's modulus $E \approx 75$ GPa and Poisson's ratio $\nu \approx 0.25$, see Figure S5). The grain size of such granite samples ranges from 0.5-1.5 mm (David et al., 1999). The samples were precut at an angle θ=30° to the largest stress axis direction. All sawcut surfaces were precision-ground and polished using a powder composed of silicon carbide particles with a diameter of 9 μm. We prepared one rough fault surface (sample R1) by sandblasting it with silicon carbide particles producing a root mean square asperity height of $Z_{rms} = 14 – 16$ μm and some long wavelength relief. In contrast, the smooth surfaces (samples S1 & S2) are characterized by $Z_{rms} \approx 3$ μm (Fig. S3).

The samples were all oven-dried for at least 48 hours before mounting strain gages. Specifically, two pairs of orthogonal strain gages attached to the center of two blocks (Fig. S1a-b) were used to measure the elastic deformation of the rock matrix. Three additional strain gages (sgf1, sgf2 and sgf3) were positioned parallel to the sawcut fault, and centered 4 mm (± 1mm) away from it. The distance between the center of two fault parallel strain gages is about 25 mm (Fig. S5). A last strain gage (sgf4) was mounted normal to fault interface in the center of samples. The strain gages were used to monitor local slip variations along the fault plane. After gluing strain gages, the samples were placed in a rubber jacket, which is used to insulate them from the oil confining medium.

An array of 16 piezoelectric transducers surrounding the samples was used to monitor Acoustic Emissions (AEs). The sensors were placed in brass housings which were glued directly on the rock using epoxy, through holes pierced in the rubber jacket (Fig. S1c). The resonant frequency of these sensors is 1 MHz, and the waveforms were recorded in a triggering mode at a sampling rate of 10 MHz. In order to locate AEs, a quasi-anisotropic velocity model composed of five horizontal layers and one vertical layer was updated every ten seconds using ultrasonic pulses transmitted between specific sensor pairs (Kwiatek et al., 2014, see Fig. S2 for details). The details on AE data processing including AE magnitude M_{AE}, b-value and focal mechanism estimations can be found in Text S1.

The prepared samples were placed in a pressure vessel (Fig. S1c) and first loaded hydrostatically up to 35 MPa. The confining pressure was then maintained constant at 35 MPa in all experiments. Samples were deformed at dry conditions using a servo-controlled hydraulic Machine Testing System (MTS 4600). Axial loading was achieved by applying vertical piston displacement rates ranging from 0.05 μm/s to 1 μm/s. A linear variable displacement transducer (LVDT) measured Δl_{LVDT}, the total displacement of the machine (with a stiffness of $K_{MTS} = 0.65 \times 10^9$ N/m or 330 MPa/mm for 5 cm diameter samples) and the specimen (stiffness of 750 MPa/mm). The differential stress ($\sigma_1 - \sigma_3$) was measured using an internal load cell with a precision of ±0.05 MPa.

Mechanical data including differential stress, axial shortening and local strains were recorded continuously at a sampling rate of 10 Hz during the experiments. To better resolve short slip episodes, a high-speed data logging system triggered by the user also recorded with sampling rates between 2 kHz (samples S1 and R1) and 5 kHz (sample S2), during short periods of interest.

In triaxial loading configuration, the average shear stress τ resolved along the inclined sawcut fault plane (angle θ to the cylinder axis) was calculated from the differential stress as:

$$\tau = (\sigma_1 - \sigma_3) \times sin\theta \times cos\theta \quad (1)$$

and the average slip s along the fault s using:

$$s = (\Delta l_{LVDT} - \Delta l_{MTS} - \Delta l_{RM})/cos\theta \quad (2)$$

where Δl_{LVDT} is the total axial displacement, Δl_{MTS} is the axial shortening of the loading machine, estimated by Δl_{MTS} =change of the axial force /K_{MTS}, and Δl_{RM} is the axial deformation of rock matrix, as given by $\Delta l_{RM} = (\varepsilon_{sgv3} + \varepsilon_{sgv4})/2 \times L$, where sgv3 and sgv4 are vertical strain gages attached to rock matrix, and L = 100 mm is the sample length. Note that the stresses are also corrected for the reduction in nominal contact area between the two parts of the fault during slip. More details about the calculations can be found in Wang et al. (2020).

3 Results

3.1 Mechanical response and AE activity

3.1.1 Smooth faults

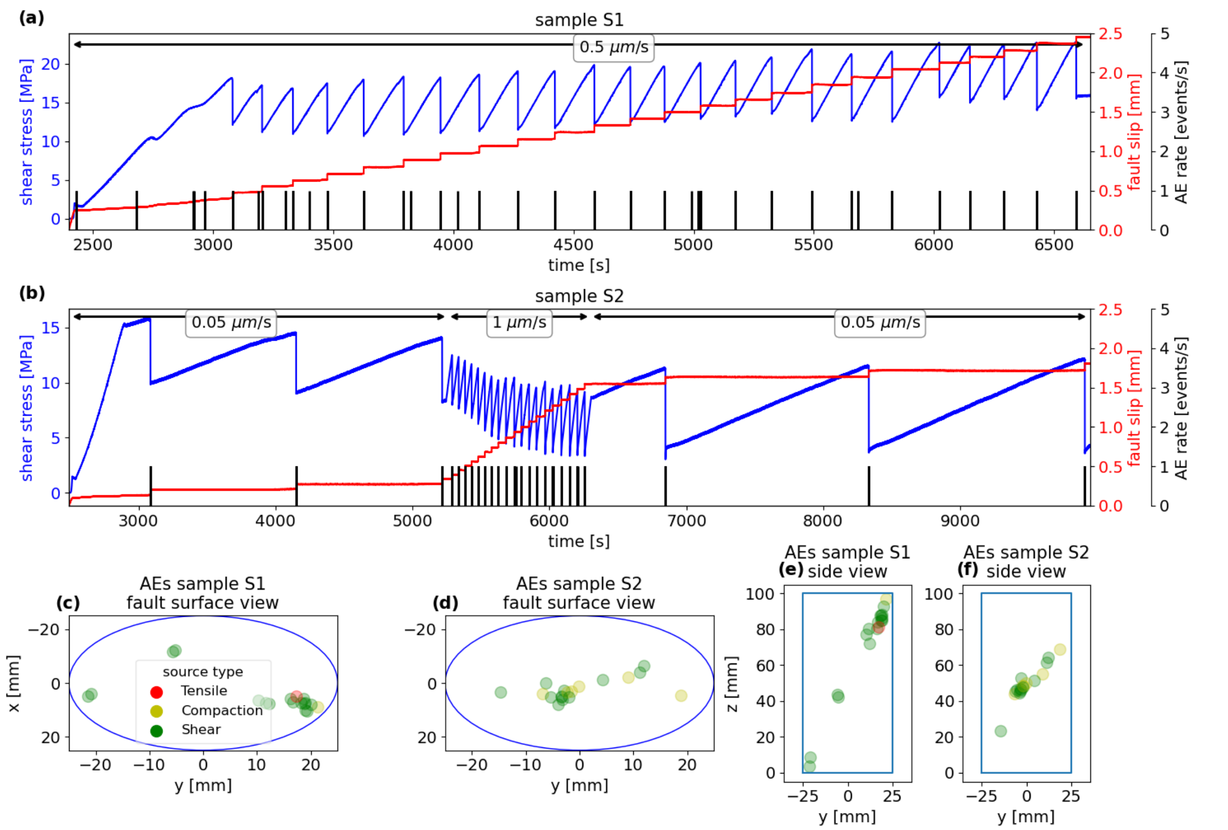

Figure 1: Evolution of shear stress, fault slip and AE rate on smooth faults (a) under a constant loading rate of 0.5 μm/s using sample S1, (b) under loading rates of 0.05 and 1 μm/s using sample S2. Acoustic emissions locations and types for (c) sample S1 fault surface view, (d) sample S2 fault surface view, (e) sample S1 side view, (f) sample S2 side view. The source types of AE hypocenter can be classified into tensile, compaction and shear focal mechanism based on P-wave first motion polarities.

The two samples with smooth sawcut faults were deformed at a constant displacement rate of 0.5 μm/s and at varying displacement rates of 0.05 μm/s and 1.0 μm/s, respectively (Fig. 1a, b). Both tests resulted in episodic stick-slip events with recurrence intervals decreasing from about 1200 s to 60 s with loading rates increasing by a factor of 20. With progressive slip, sample S1 showed a small increase in peak stress for the stick-slip events, possibly due to progressive gouge formation. The stress drop magnitude associated with the stick-slip events tends to increase with cumulative fault slip, and ranges from 5 MPa for the smallest event of sample S2 at 1 μm/s (see Fig. 1b), to 9 MPa for the largest stick-slip event on sample S1, loaded at 0.5 μm/s (see Figure 1a). In contrast, increasing loading rates from 0.05 μm/s to 1.0 μm/s showed a reduction in peak stress from 15 MPa to about 10 MPa. This was accompanied by a decrease of stress drop magnitude from 7 MPa to 5 MPa (Figure 1b).

In general, preparatory slip on smooth faults is small and failure occurs abruptly (i.e. the main slip episode lasts about 2 ms, see Fig. 4b). Additionally, we did not resolve any time delay between the different strain gage signals sampled at frequencies up to 5 kHz. Considering the spacing of 2.5 cm between the strain gages (Fig. S2), and assuming a rupture front propagating in the fault plane along the fault strike direction (see Fig. S1b), this would result in rupture velocities V_r larger than 125 m/s. During the elastic loading of the locked smooth faults, we observed very little AE activity. However, every single stick-slip event was accompanied by a very large AE, and by an audible sound. Large AE events' timings correspond to the time of the main stress drop ± 100 ms, within the accuracy of the synchronized data acquisition systems. These AEs have large and typically clipped waveforms that last several milliseconds. The AE hypocenters of these large events were located on the sawcut faults partly forming localized clusters (Fig.1c-f). Based on P-wave first motion polarities (Zang et al., 1998), the AEs display predominantly double-couple shear mechanisms.

3.1.2 Rough fault

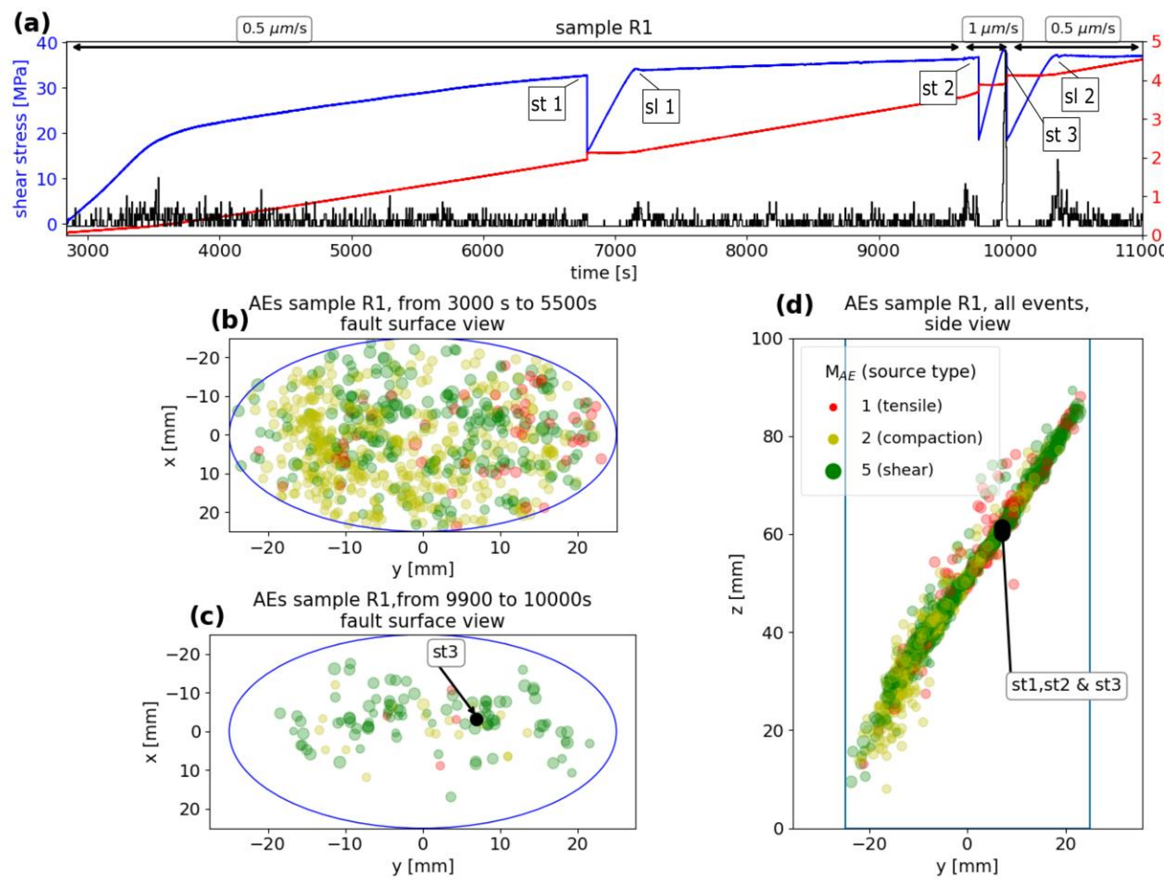

Figure 2: (a) Evolution of shear stress, fault slip and acoustic emission rate on a rough fault under loading rates of 0.5 and 1 μm/s using sample R1. (b) Fault surface view of corresponding AEs locations and types at the start of the experiment, before the first stick-slip st1. (c) AEs locations over the fault surface and their source types after the second stick-slip st2, and until stick-slip st3. (d) Side view of all located AEs during the experiment. The black dots indicate the location of the AEs associated with the main stick-slip events. Note that the size of each dot is positively correlated with the amplitude of an AE event. The source types of AE hypocenter can be classified into tensile, compaction and shear focal mechanism based on P-wave first motion polarities.

Loading of the sample containing a rough fault resulted in significantly different deformation compared to smooth faults. Beyond a yield stress, the sample assembly shortened by continuous sliding along the sawcut fault. At a piston displacement rate of 0.5 μm/s the samples showed stable sliding for about 1.5 mm and hardening with strength increasing by about 10 MPa. Sliding was accompanied by prominent AE activity reaching a total 1595 events before a sudden stick-slip event (st1) occurred (Fig. 2a). AEs were aligned with the sawcut fault and distributed across the entire fault surface (Fig. 2b-d). Initially, during stable slip AEs were dominated by small-magnitude compaction events (Fig. 2b and S9c), progressively replaced by shear events and few tensile source types (cf. similar AEs microkinematic behavior for stick-slip experiments at higher confining pressure in Kwiatek, Goebel, et al., 2014). The first stick-slip (st1) occurred after about 2 mm of stable sliding, with a stress drop of about 16 MPa, terminating the first phase of the test. We note that the AE activity did not increase significantly prior to failure.

After event st1 the fault was locked again and elastic loading resumed to a yield point at a shear stress of about 32 MPa (sl1), which is roughly similar to the peak stress reached before the stick-slip event st1 occurred. Stable fault slip initiated at a peak shear stress of 34 MPa and the fault strengthened again but at a smaller rate. This sliding episode lasted until the displacement rate was increased to 1 μm/s. Shortly after the displacement rate was increased, two stick-slips occurred (st2 and st3) with stress drops of about 15-20 MPa. Both stick-slip events were preceded by bursts in AE activity.

After the stick-slip event st3, the loading was reset to a displacement rate of 0.5 μm/s. The sawcut was locked and loading reached a peak stress of 38 MPa beyond which a small slow slip event (sl2) initiated a third stable sliding phase. This suggests that the transition to unstable behavior at the loading rate of 1 μm/s is a result of the increased loading rate rather than of the surface evolution by cumulative slip. Note that slow slip sl2 is preceded by a burst of AEs similar to the one preceding stick-slip event st2, showing that bursts in AEs are not necessarily followed by rapid stick-slip events.

Overall, the located AEs align well with the fault plane (Fig. 2d). In a 100 seconds time window just before stick-slip events we observed a relatively dispersed population of AEs which however concentrate on local higher stress areas (Fig. 2c and S4). In general, the AE events occurring shortly before stick-slip events and slow slip events display larger amplitudes and are dominantly shear focal mechanism. A few compaction events remain smaller in comparison.

The magnitude-frequency distribution of AEs shows a continuous trend of decreasing *b*-value towards the final stick slip event st3 (Fig. S9). This trend is punctuated by short episodes of rapid *b*-value decrease likely associated with local slip events (Dresen et al., 2020).

3.2 Preparatory slip

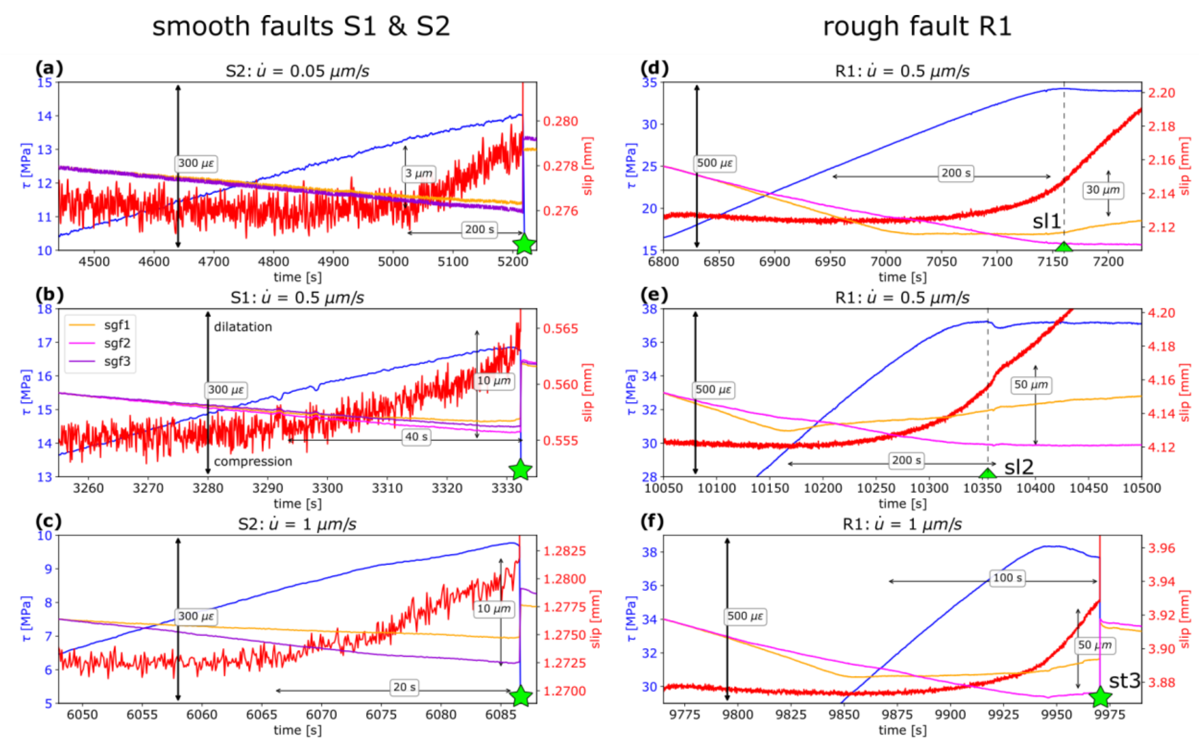

Figure 3: Evolution of shear stress (blue curve), slip (red curve) and available fault parallel strain gage signals (purple, pink and yellow curves), during selected phases of the rock deformation experiments. (a-c) Selected stick-slips for smooth faults S1 and S2 at loading rates of (a) $\dot{u}$= 0.05 μm/s, (b) 0.5 μm/s and (c) 1 μm/s. (d,e) Slow-slip events sl1 (d) and sl2 (e) at a loading rate of $\dot{u}$= 0.5 μm/s on the rough fault. (f) Stick-slip st3 on the rough fault R1, loaded at $\dot{u}$= 1 μm/s. The strain signals are offset to zero at the start of the plots, upwards corresponds to dilatation while downwards corresponds to compression. The strain amplitude in με is indicated on each plot. Stick-slip onsets are indicated by green stars, and slow slip onsets, corresponding to the start of shear stress decrease, are indicated by green triangles.

3.2.1 Smooth faults

Here we focus on the preparatory aseismic slip prior to stick-slips on smooth sawcut faults at different background loading rates (Fig. 3a-c), showing a few representative stick-slip events in greater detail. Macroscopic slip (Eq. -2) corresponds to the average displacement between the two fault blocks. After stick-slip events, the smooth faults were locked and loading resulted in elastic deformation of the bulk sample (e.g. Fig. 3a, 4500-5000s). Beyond a yield point, slip initiated, eventually leading to failure. The total amount of fault slip for the smooth faults (Z_{rms} ≈ 3 μm) during this preparatory phase is estimated to be about 3-10 μm. The duration of the preparatory phase decreased with increasing loading rate, from about 200 s at 0.05 μm/s, to 40 s at 0.5 μm/s, and 20 s at 1 μm/s (Fig. 3a-c).

Within 10 s before failure (see Fig. S6a-c), we observed that the fault parallel strain gage signals started diverging a few seconds before the stick-slips. At a loading rate of 0.5 μm/s, the shear stress started dropping roughly one second before the slip event. At a loading rate of 1 μm/s shear stress decreased approximately 0.5 s before failure. At a low loading rate of 0.05 μm/s, this weakening phase is just barely observable due to moderate mechanical noises visible on stress, slip and deformation signals (Fig. S6a).

3.2.2 Rough faults

Preparatory slip before slow and fast slip events on the rough fault ($Z_{rms} \approx 14$ μm) showed a more complex behavior (Fig. 3d-f). For example, stick-slip events st1 and st2 occurred quasi-instantaneously without visible slip acceleration, irrespective of doubling the loading rate between events (Fig. S6d-f). This is in contrast to stick-slip st3 and slow slip sl1 and sl2 (Fig. 3d-f). The preparatory phase lasting approximately 200 s corresponds to an amount of slip up to roughly 50 μm (5 times the slip observed on the smooth fault at the same loading rate) for the two slow slip events sl1, sl2. Prior to stick-slip st3 at a loading rate of 1 μm/s, preparatory slip duration was reduced to 100 s, while the slip amount remained about 50 μm (st3, Fig. 3f). Interestingly, the start of preparatory slip seems to correspond to some local slip detected on the strain signal of sgf1 (Fig. 3d-f), while strain gage sgf2 remains in compression.

Prior to stick-slip st2 (Fig. S6e, f), no such preparatory slip acceleration could be observed as the fault was not ‘sealed/locked’ by a previous stick-slip, but instead the fault was creeping continuously. However, we observe that the increase of loading rate from 0.5 to 1 μm/s (Fig. S6e, around 9640 s), caused strong shear stress instabilities before triggering the main stick-slip. Zooming in events st1 (Fig. S6d) and st2 (Fig. S6f), for which the fault continuously creeps and is driven by the load point velocity (v_{lp}), we do not resolve any clear precursory signal prior to failure. The precursory stress variations might be much smaller than the large stress oscillations observed during a few tens of seconds preceding the events.

3.2.3 Scaling of the preparatory slip with loading rate and roughness

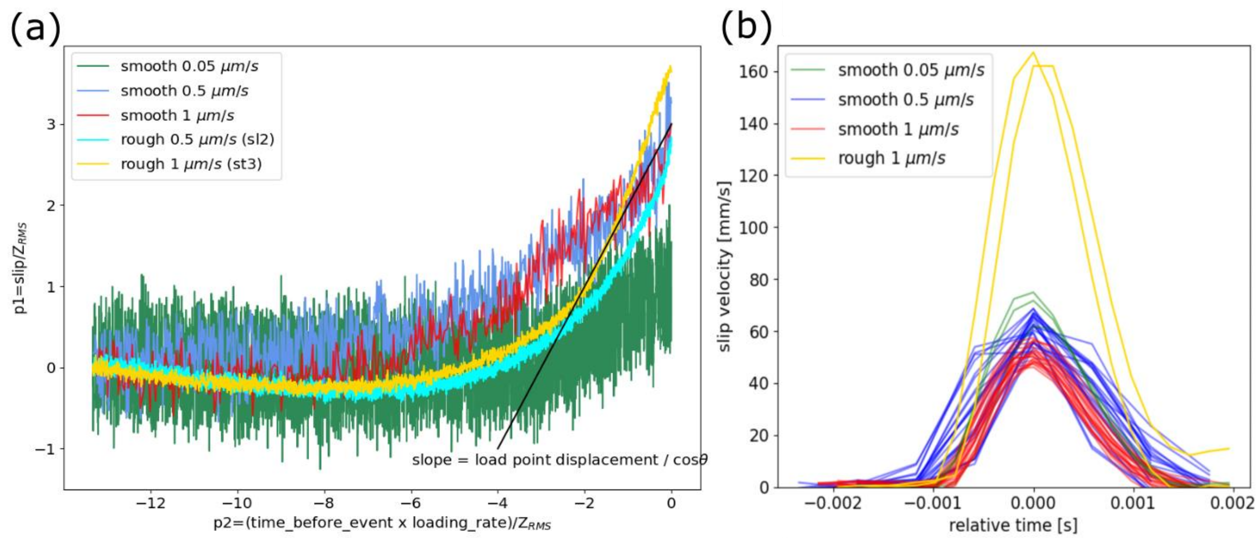

Figure 4: (a) Dimensionless plot of slip normalized by roughness versus the time to events (instability) normalized by loading rate and roughness (Z_{rms}). The slope corresponding to the load point displacement projected on the fault plane is indicated by a solid black line. (b) Average slip velocity between the fault blocks recorded during stick-slip events on smooth faults at loading rates of 0.05 μm/s, 0.5 μm/s and 1 μm/s, and the rough fault at a loading rate of 1 μm/s.

The preparatory slip displacement depends on roughness and the duration of the preparatory slip phase depends on both roughness and loading rate. To compare the data from the different tests we plot the non-dimensional parameters p1=*slip*/Z_{rms} and p2 = (*time-to-event* × *loading-rate)*/Z_{rms}. Although we observe that this scaling works rather well for the total normalized slip amount (except for the smooth fault at the loading rate of 0.05 μm/s where the scaled slip is approximately half the slip amount observed at other loading rates), the shape of the curves for smooth and rough faults are different. The slip on smooth faults increases at a low rate accounting for only a fraction (10 % - 30 %) of the load point velocity (0.1-0.3 v_{lp}, see Fig. S11). For the rough fault at the loading rate of 0.5 μm/s, preparatory slip clearly accelerated following the growth trend of 1/(time to failure). On the same rough fault, prior to stick-slip event st3 at the loading rate of 1 μm/s, slip evolution accelerates as 1/(time to failure) before reaching v_{lp} , and slightly exceeding it at failure (see Fig. 4a and S8).

3.2.4 Slip velocity associated with the stress drop during stick-slip events

During the co-seismic stage of stick-slip we measured the average magnitudes of slip and stress drop along the fault plane by using the recordings of axial force, displacement and deformation values at the edges of samples (see Section 2). In Fig. 4b, we looked at the slip velocities during the short phase where most of the slip occurs, when the high-speed data is available. For both smooth and rough faults this phase lasted about 2 ms. At a loading rate of 1 μm/s, the smooth fault S2 slipped with velocities between 45 to 55 mm/s, the stress drop was around 4.5 to 6 MPa and the slip around 60 μm (Fig. S7). For comparison, the preparatory slip velocity on smooth faults ranged from 0.005 μm/s to 0.45 μm/s, at load point displacement rates of 0.05 μm/s and 1 μm/s, respectively. The total preparatory slip was around 10 μm, accounting for about 15% - 20% of the displacement measured during stick-slip events. At a loading rate of 1 μm/s on the rough fault, the slip velocity reached 160 mm/s, the stress drop 18-19 MPa, and the slip was around 200 μm (4 times the amount of preparatory slip). In these experiments, the slip velocity increased with decreasing loading rate, with values larger than 70 mm/s at 0.05 μm/s. Slip velocity was also strongly correlated with stress drop (Fig. S10). When plotting shear stress versus slip (Fig. S7), we obtained the fault stiffness of $K \approx 85$ MPa/mm for the smooth faults, and $K \approx 95$ MPa/mm for the rough fault.

4 Discussion

The results of this study provide new insights into the preparatory and nucleation phase of seismic ruptures and factors controlling frictional instabilities at the laboratory scale. In particular, we stress the important role of fault roughness and loading rate for the transition to dynamic failure at elevated confining pressures. The preparatory slip phase prior to failure shows major differences between smooth and rough faults. The average fault slip, local strain variations, and the evolution of AE characteristics clearly depend on roughness. In general, our observations showed dominantly stable slip of rough faults at 35 MPa confining pressure and at load point displacement rate of 0.5 μm/s. In contrast, smooth sawcut faults produced multiple stick-slips at similar conditions. This is in good agreement with results from previous studies (e.g. Morad et al., 2022; Okubo & Dieterich, 1984).

A plethora of studies showed that roughness of faults plays an important role in controlling fault stability (Ohnaka, 2003, Ohnaka and Shen 1999, Harbord et al., 2017; Morad et al., 2022; Okubo & Dieterich, 1984, Scholz, 1988). Okubo & Dieterich (1984) showed that the critical slip-weakening distance D_c over which the stress reaches its residual level increases with roughness. This means that the critical patch size or nucleation length required for a rupture to reach instability and accelerate to a dynamic rupture is larger for rough faults, assuming a constant stress drop. Also, the preparatory slip is expected to increase with roughness, which is in good agreement with our observations since we find that the average slip amount during the yielding phase prior to stick-slip events scales with roughness (Fig. 4a). Note that decreasing roughness does not always promote instability, as very smooth faults ($Z_{rms} < 1$ μm) were found to also exhibit stable behavior (Morad et al., 2022) and rough faults can become unstable at very high confining pressures (Harbord et al., 2017).

All stick-slip events observed for smooth and rough samples were accompanied by an audible noise likely caused by the propagation of a dynamic rupture. In the framework of slip-weakening friction law, the critical nucleation length L_c for dynamic rupture has been estimated by Uenishi & Rice (2003) as:

$$L_c = 1.158\ {}^{G}\!/_{K_f} \tag{3}$$

where G is shear modulus and K_f is slip weakening rate (here equivalent to calculation of fault stiffness). We estimated an average value of K_f of 90 MPa/mm and G = 30 GPa for La Peyratte granite. A similar estimate for a circular patch with the critical radius R_c was given by Day (1983):

$$R_c = 7\pi/24\ {}^{G}\!/_{K_f}. \tag{4}$$

The estimates for the critical nucleation length using Eq. 3 and Eq. 4 give 39 cm and 30 cm, respectively. Both estimates exceed the sample size suggesting that dynamic slip should not occur in stark contrast to our observations. We posit that this discrepancy may be due to the nature of the failure process. We suggest that the stress drop occurs very rapidly over a short slip distance that is not captured by the data acquisition system sampling force and displacement in the far-field, with maximum rates of 2 and 5 kHz, respectively. This indicates that most of the slip lasting about 2 ms is accommodated by frictional sliding. As discussed in Paglialunga et al., (2021), the stress versus slip evolution measured likely represents a long-tail process over a slip distance that is much larger than the critical slip-weakening distance *Dc* associated with rapid initial stress drop (by a factor 50 in Paglialunga et al., 2021), and which controls rupture nucleation.

We find that recorded stick-slip duration for all events is similar (around 2 ms) as observed previously in stick-slip tests performed with constant machine stiffness. This implies a linear relation between slip rate (particle velocity) and stress drop (Johnson & Scholz, 1976) as also suggested theoretically by Brune (1970). Our results also show that stress drop correlates with maximum slip rates (Fig. S10). It explains the larger slip rates recorded on rough faults for which the stress drop is also larger compared to smooth faults. This larger stress drop, although influenced by the loading rate, is probably primarily controlled by the peak friction which is also larger on the rough fault, in agreement with previous studies (Ohnaka, 1973).

Increasing the loading rate on rough faults (from 0.5 μm/s to 1 μm/s) clearly promotes instability, as previously observed under lower pressure conditions (Guérin-Marthe et al., 2019; Kato et al., 1992; McLaskey & Yamashita, 2017). Increasing load point velocity from 0.05 μm/s to 1 μm/s on smooth faults reduced stress drop $\Delta\tau$ of stick-slip events from 7 MPa to 5 MPa. Also, increasing loading rate by a factor 20 reduces average slip rates from 70-75 mm/s to 45-55 mm/s. This suggests that increasing the loading rate of smooth fault surfaces in granite does not necessarily promote unstable slip. This is in contrast with the observations on rough faults. Although as discussed by Guerin-Marthe (2019) instabilities could be suppressed if the contacts do not have the time to re-strengthen under a sustained high loading rate, it does not seem to apply here. However, as cumulative slip increases under a loading rate of 1 μm/s, the stress drops of stick-slip events increased as well, suggesting rather that cumulative slip might be also influencing the stability of smooth faults.

Preparatory slip on rough faults is accompanied by numerous AEs with activity increasing prior to stick slip events (Fig. S8 and Fig. 3a, st2, st3). The AEs are distributed across the fault but approaching failure, larger events concentrate on long wavelength fault asperities possibly concentrating local stresses (Goebel et al., 2012). The AE activity preceding the failure starts when an increase in slip rate is observed, in cases coinciding with macroscopic yielding or very small stress drops (Dresen et al., 2020; McLaskey & Lockner, 2014, see Fig. S8). We also observe diverging strain gage signals located along the faults displaying that slip is heterogeneous in space and time. In general, this heterogeneity is also manifested by short episodes of significant *b*-value fluctuations during stable slip superimposed on a general trend of decreasing *b*-value (Fig. S9).

From the combined mechanical data and AE characteristics of the rough fault experiment, a complex slip pattern emerges. It suggests spatio-temporally distributed slip patches along the surface, which are growing/coalescing with cumulative slip, while the fault blocks are macroscopically slipping at the load point velocity. A large amount of slip is needed in order to redistribute stresses (by breaking asperities) and create a critical slip patch causing instability. The coalescence of slipping patches would agree with the acceleration of preparatory slip with time observed for the rough faults when they are previously locked. This could also help explaining the loading rate role in promoting instabilities at 1 μm/s. Indeed, under a low loading rate, if enough asperities are able to re-strengthen, while others are broken, then the fault can slip continuously in a stable fashion. However, as the re-strengthening of contacts is not only slip-dependent, but also time-dependent (Dieterich & Kilgore, 1994), increasing loading rate could also rise the proportion of weak/broken versus strong contacts, and therefore increases the likelihood of having a large slipping patch close to the critical size for dynamic rupture.

On smooth faults, the behavior is different. First, almost no AEs are detected during the preparatory phase, from the onset of yielding until the stick-slip. This is a possible effect of the small elevation of contacts which upon breaking do not necessarily trigger AEs above the noise level, and is generally comparable to what has been observed for stick-slip experiment on smooth faults in Kwiatek, Goebel, et al. (2014). Then, we observe that smooth faults are always unstable with regular stick-slip events, for the whole range of load point velocities applied (0.05-1 μm/s). We argue that on smooth faults, once a slipping patch or crack has formed, the stress increase at its tips might be sufficient to break the small contacts immediately surrounding it. A slipping zone could therefore expand and accelerate relatively easily, reaching dynamic rupture velocities. In comparison, if an asperity breaks or a patch starts slipping on a rough fault, there might be strong contacts preventing further growth, and the next asperity to break might not be an adjacent one. As long as the slipping patches are not able to merge reaching the critical length for instability, we might expect stable sliding.

Conflict of Interest

The authors declare no conflicts of interest relevant to this study.

Data Availability Statement

The data used in this manuscript are available online (https://doi.org/10.5281/zenodo.6411819).

Acknowledgments

S.G-M and P.M.G. acknowledge funding from the Helmholtz Association in the frame of the Young Investigators Group VH-NG-1232 (SAIDAN). The authors would also like to thank Michael Naumann and Stefan Gehrmann for the technical help, and Laboratoire Colas Centre Ouest for providing the La Peyratte granite samples.

References

Bouchon, M., Durand, V., Marsan, D., Karabulut, H., & Schmittbuhl, J. (2013). The long precursory phase of most large interplate earthquakes. *Nature Geoscience*, *6*(4), 299–302. https://doi.org/10.1038/ngeo1770

Brune J.N. (1970). Tectonic stress and the spectra of seismic shear waves from earthquakes. *J Geophys Res*, *75*(26). https://doi.org/10.1029/jb075i026p04997

David, C., Menéndez, B., & Darot, M. (1999). Influence of stress-induced and thermal cracking on physical properties and microstructure of La Peyratte granite.

International Journal of Rock Mechanics and Mining Sciences, *36*(4). https://doi.org/10.1016/S0148-9062(99)00010-8

Day, S. M. (1983). Three-dimensional simulation of spontaneous rupture: The effect of nonuniform prestress. *International Journal of Rock Mechanics and Mining Sciences & Geomechanics Abstracts*, *20*(5). https://doi.org/10.1016/0148-9062(83)90099-2

Dieterich, J. H., & Kilgore, B. D. (1994). Direct observation of frictional contacts: New insights for state-dependent properties. *Pure and Applied Geophysics PAGEOPH*, *143*(1–3). https://doi.org/10.1007/BF00874332

Dresen, G., Kwiatek, G., Goebel, T., & Ben-Zion, Y. (2020). Seismic and Aseismic Preparatory Processes Before Large Stick–Slip Failure. *Pure and Applied Geophysics*, *177*(12), 5741–5760. https://doi.org/10.1007/s00024-020-02605-x

Durand, V., Bentz, S., Kwiatek, G., Dresen, G., Wollin, C., Heidbach, O., et al. (2020). A two-scale preparation phase preceded an Mw 5.8 earthquake in the Sea of Marmara Offshore Istanbul, Turkey. *Seismological Research Letters*, *91*(6), 3139–3147. https://doi.org/10.1785/0220200110

Ellsworth, W. L., & Beroza, G. C. (1995). Seismic Evidence for an Earthquake Nucleation Phase. *Science*. https://doi.org/10.1126/science.268.5212.851

Font, Y., Kao, H., Lallemand, S., Liu, C. S., & Chiao, L. Y. (2004). Hypocentre determination offshore of eastern Taiwan using the maximum intersection method. *Geophysical Journal International*, *158*(2). https://doi.org/10.1111/j.1365-246X.2004.02317.x

Goebel, T. H. W., Becker, T. W., Schorlemmer, D., Stanchits, S., Sammis, C., Rybacki, E., & Dresen, G. (2012). Identifying fault heterogeneity through mapping spatial anomalies in acoustic emission statistics. *Journal of Geophysical Research: Solid Earth*, *117*(3). https://doi.org/10.1029/2011JB008763

Guerin-Marthe, S. (2019). Analogue and numerical models of earthquake rupture, *Chapter 5*, 218. Retrieved from http://etheses.dur.ac.uk/13341/

Guérin-Marthe, S., Nielsen, S., Bird, R., Giani, S., & di Toro, G. (2019). Earthquake Nucleation Size: Evidence of Loading Rate Dependence in Laboratory Faults. *Journal of Geophysical Research: Solid Earth*, *124*(1). https://doi.org/10.1029/2018JB016803

Guo, Z., & Ogata, Y. (1997). Statistical relations between the parameters of aftershocks in time, space, and magnitude. *Journal of Geophysical Research: Solid Earth*, *102*(B2). https://doi.org/10.1029/96jb02946

Harbord, C. W. A., Nielsen, S. B., de Paola, N., & Holdsworth, R. E. (2017). Earthquake nucleation on rough faults. *Geology*, *45*(10), 931–934. https://doi.org/10.1130/G39181.1

Johnson, T. L., & Scholz, C. H. (1976). Dynamic properties of stick-slip friction of rock. *Journal of Geophysical Research*, *81*(5). https://doi.org/10.1029/jb081i005p00881

Karner, S. L., & Marone, C. (2000). Effects of loading rate and normal stress on stress drop and stick-slip recurrence interval. In *Geophysical Monograph Series* (Vol. 120). https://doi.org/10.1029/GM120p0187

Kato, A., & Ben-Zion, Y. (2021). The generation of large earthquakes. *Nature Reviews Earth & Environment*, *2*(1), 26–39. https://doi.org/10.1038/s43017-020-00108-w

Kato, A., Obara, K., Igarashi, T., Tsuruoka, H., Nakagawa, S., & Hirata, N. (2012). Propagation of slow slip leading up to the 2011 Mw 9.0 Tohoku-Oki earthquake. *Science*, *335*(6069). https://doi.org/10.1126/science.1215141

Kato, N., Yamamoto, K., Yamamoto, H., Hirasawa, T., Aki, K., Ohnaka, M., et al. (1992). *Strain-rate effect on frictional strength and the slip nucleation process*.

Kwiatek, G., Charalampidou, E. M., Dresen, G., & Stanchits, S. (2014). An improved method for seismic moment tensor inversion of acoustic emissions through assessment of sensor coupling and sensitivity to incidence angle. *International Journal of Rock Mechanics and Mining Sciences*, *65*. https://doi.org/10.1016/j.ijrmms.2013.11.005

Kwiatek, G., Goebel, T. H. W., & Dresen, G. (2014). Seismic moment tensor and b value variations over successive seismic cycles in laboratory stick-slip experiments. *Geophysical Research Letters*, *41*(16). https://doi.org/10.1002/2014GL060159

Latour, S., Schubnel, A., Nielsen, S., Madariaga, R., & Vinciguerra, S. (2013). Characterization of nucleation during laboratory earthquakes. *Geophysical Research Letters*, *40*(19). https://doi.org/10.1002/grl.50974

Marone, C. (1998). The effect of loading rate on static friction and the rate of fault healing during the earthquake cycle. *Nature*, 69–72.

McLaskey, G. C. (2019). Earthquake Initiation From Laboratory Observations and Implications for Foreshocks. *Journal of Geophysical Research: Solid Earth*, *124*(12). https://doi.org/10.1029/2019JB018363

McLaskey, G. C., & Lockner, D. A. (2014). Preslip and cascade processes initiating laboratory stick slip. *Journal of Geophysical Research: Solid Earth*, *119*(8). https://doi.org/10.1002/2014JB011220

Mclaskey, G. C., & Yamashita, F. (2017). Slow and fast ruptures on a laboratory fault controlled by loading characteristics. *Journal of Geophysical Research: Solid Earth*, *122*(5), 3719–3738. https://doi.org/10.1002/2016JB013681

Morad, D., Sagy, A., Tal, Y., & Hatzor, Y. H. (2022). Fault roughness controls sliding instability. *Earth and Planetary Science Letters*, *579*. https://doi.org/10.1016/j.epsl.2022.117365

Nelder, J. A., & Mead, R. (1965). A Simplex Method for Function Minimization. *The Computer Journal*, *7*(4). https://doi.org/10.1093/comjnl/7.4.308

Ohnaka, M. (1973). Experimental studies of stick-slip and their application to the earthquake source mechanism. *Journal of Physics of the Earth*, *21*(3). https://doi.org/10.4294/jpe1952.21.285

Okubo, P. G., & Dieterich, J. H. (1984). Effects of physical fault properties on frictional instabilities produced on simulated faults. *Journal of Geophysical Research*, *89*(B7), 5817–5827. https://doi.org/10.1029/JB089iB07p05817

Paglialunga, F., Passelègue, F., Brantut, N., Barras, F., Lebihain, M., & Violay, M. (2021). On the scale dependence in the dynamics of frictional rupture: constant fracture energy versus size-dependent breakdown work.

Passelègue, F. X., Almakari, M., Dublanchet, P., Barras, F., Fortin, J., & Violay, M. (2020). Initial effective stress controls the nature of earthquakes. *Nature Communications*, *11*(1). https://doi.org/10.1038/s41467-020-18937-0

Rice, J. R. (1983). Constitutive relations for fault slip and earthquake instabilities. *Pure and Applied Geophysics PAGEOPH*, *121*(3). https://doi.org/10.1007/BF02590151

Ross, Z. E., Meier, M. A., & Hauksson, E. (2018). P Wave Arrival Picking and First-Motion Polarity Determination With Deep Learning. *Journal of Geophysical Research: Solid Earth*, *123*(6). https://doi.org/10.1029/2017JB015251

Ruiz, S., Metois, M., Fuenzalida, A., Ruiz, J., Leyton, F., Grandin, R., et al. (2014). Intense foreshocks and a slow slip event preceded the 2014 Iquique Mw8.1 earthquake. *Science*, (6201), 1165–1169. https://doi.org/10.1126/science.1256074

Shi, Y., & Bolt, B. A. (1982). The standard error of the magnitude-frequency b value . *Bulletin of the Seismological Society of America*, *72*(5). https://doi.org/10.1785/bssa0720051677

Stanchits, S., Mayr, S., Shapiro, S., & Dresen, G. (2011). Fracturing of porous rock induced by fluid injection. *Tectonophysics*, *503*(1–2). https://doi.org/10.1016/j.tecto.2010.09.022

Tape, C., Holtkamp, S., Silwal, V., Hawthorne, J., Kaneko, Y., Ampuero, J. P., et al. (2018). Earthquake nucleation and fault slip complexity in the lower crust of central Alaska. *Nature Geoscience*, *11*(7). https://doi.org/10.1038/s41561-018-0144-2

Uenishi, K., & Rice, J. R. (2003). Universal nucleation length for slip-weakening rupture instability under nonuniform fault loading. *Journal of Geophysical Research: Solid Earth*, *108*(B1). https://doi.org/10.1029/2001JB001681

Wang, L., Kwiatek, G., Rybacki, E., Bonnelye, A., Bohnhoff, M., & Dresen, G. (2020). Laboratory Study on Fluid-Induced Fault Slip Behavior: The Role of Fluid Pressurization Rate. *Geophysical Research Letters*, *47*(6). https://doi.org/10.1029/2019GL086627

Yamashita, F., Fukuyama, E., Xu, S., Kawakata, H., Mizoguchi, K., & Takizawa, S. (2021). Two end-member earthquake preparations illuminated by foreshock activity on a meter-scale laboratory fault. *Nature Communications*, *12*(1). https://doi.org/10.1038/s41467-021-24625-4

Zang, A., Wagner, F. C., Stanchits, S., Dresen, G., Andresen, R., & Haidekker, M. A. (1998). Source analysis of acoustic emissions in Aue granite cores under symmetric and asymmetric compressive loads. *Geophysical Journal International*, *135*(3). https://doi.org/10.1046/j.1365-246X.1998.00706.x

Zhuo, Y.-Q., Liu, P., Guo, Y., Chen, H., Chen, S., & Wang, K. (2022). Cross-effects of loading rate and cumulative fault slip on pre-seismic rupture and unstable slip rate of laboratory earthquakes. *Tectonophysics*, *826*, 229266. https://doi.org/10.1016/j.tecto.2022.229266

Geophysical Research Letters

Supporting Information for

Preparatory Slip in Laboratory Faults: Effects of Roughness and Loading Rate

Simon Guérin-Marthe[1], Grzegorz Kwiatek[1], Lei Wang[1], Audrey Bonnelye[1,2], Patricia Martínez-Garzón[1], Georg Dresen[1,3]

[1]Helmholtz Centre Potsdam, GFZ German Research Centre for Geosciences, Section 4.2 Geomechanics and Scientific Drilling, Potsdam, Germany.
[2]Free University Berlin, Berlin, Germany
[3]University of Potsdam, Potsdam, Germany

Contents of this file

Introduction

The complementary material of the article includes:

- The description of Acoustic Emissions (AEs) processing (Text S1)
- The roughness characterization of the fault surfaces (Fig. S1)
- The sensor setup (Fig. S2)
- The scans of the sandblasted sawcut surfaces (Fig. S3)
- The acoustic emission locations prior a stick-slip event, superimposed to the topography of the rough fault (Fig. S4)
- Stress vs strain curve for estimating the Young's modulus of the La Peyratte granite samples. (Fig. S5)
- The stress, slip and strain evolution during a few seconds prior to selected stick-slip events on rough and smooth faults (Fig. S6)
- The fault stiffness estimation (Fig. S7)
- A zoom on stick-slip events on the rough fault, with the acoustic emission locations (Fig. S8)
- The b-value evolution during the experiment on the rough fault (Fig. S9)
- The relation between stress drop and maximum slip velocity (Fig. S10)
- A comparison between the slip velocity during the preparatory phase of smooth faults and the load point velocity (Fig. S11)

Text S1.

Full AE waveforms, as well as active ultrasonic transmission measurements were recorded at a sampling rate of 10 MHz with 16-bit amplitude resolution using the 16-channels DAXBox (Prökel) recording system. The full waveform recordings were first separated into AE events and UT measurements using an automated procedure. Active ultrasonic transmission (UT) measurements were performed every 10 seconds throughout the whole experiment. P-wave travel times were first picked using the Akaike information criterion (AIC) criterion and corrected for the sample deformation and fault slip. These travel times were then used to calculate time-dependent quasi-anisotropic *P*-wave velocity model composed of 5 layers perpendicular to and 1 vertical layer parallel to loading axis (see e.g., Stanchits et al. 2011; Kwiatek et al. 2014). The recordings of AE events were first amplified by 40 dB and high-pass filtered at 100 kHz (Physical Acoustic Corporation). *P*-wave arrival times were automatically picked using the convolutional neural network-type picker based on Ross et al., (2018) picker trained on AE experiments. To locate AEs, the Equivalent Differential Time method (e.g., Font et al., 2004) was used and solved using a combination of grid search followed by simplex (e.g. Nelder and Mead, 1965) optimization algorithms while using the time-dependent velocity model derived earlier from UT data. The average AE hypocenter location accuracy is ± 2 mm (Stanchits et al., 2011).

After hypocenter determination, the relative AE magnitude was estimated as:

$$M_{\mathrm{AE}} = \log_{10}\sqrt{\frac{1}{n}\sum_{i=1}^{n}(A_i R_i)^2},$$

where A_i and R_i are the first P-wave amplitude and source-receiver distance for each individual AE sensor i, respectively (e.g. Dresen et al., 2020; Zang et al., 1998). We note this magnitude reveals relative size differences between AE events and is not directly calibrated to the physical size of the events (see e.g. Dresen et al., 2020 for additional discussion). Finally, polarity coefficient has been calculated for each AE event following Zang et al. (1998):

$$p_{\mathrm{AE}} = \frac{1}{n}\sum_{i=1}^{n}\mathrm{sgn}(A_i),$$

using average polarity of first P-wave amplitudes (cf. Figure S9c). This parameter signifies whether the AE events microkinematics reflects material compaction, tensile opening or shearing (see Zang et al. 1998 for details).

Using the catalog of located AE events above the AE magnitude of completeness of $M_{AE}^{C} = 1.8$ (assessed by visual inspection of magnitude-frequency distribution) we calculated the magnitude-frequency Gutenberg Richter b-value in a moving time window of 200 seconds (Figure S9b). For each window, the b-value has been estimated using the maximum likelihood approach:

$$b = \frac{1}{\overline{M_{\mathrm{AE}}} - M_{\mathrm{AE}}^{C}}\log_{10}(e),$$

where $\overline{M_{AE}}$ is the average magnitude of events above magnitude of completeness. The estimates have been corrected for the bin size (e.g. Guo & Ogata, 1997). The uncertainties of *b*-value have been estimated following Shi & Bolt (1982), suitable for weakly non-stationary catalogs.

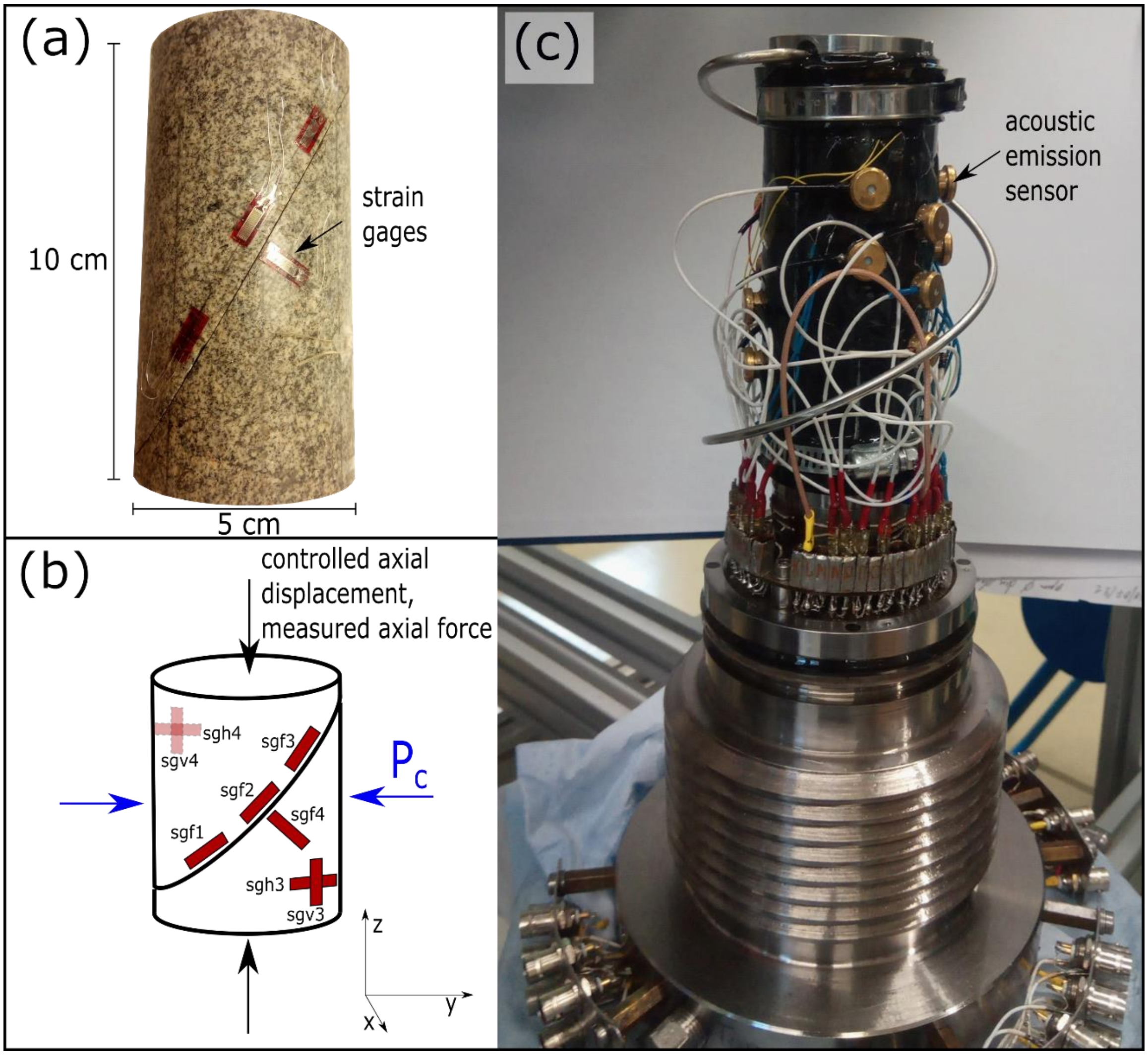

Figure S1. (a) Photography of the sawcut granite blocks with the strain gages glued directly on the sample. (b) Schematic view of the strain gages configuration and of the loading forces. (c) Specimen assembly with the AE sensors placed in brass casings mounted directly on the sample by filling holes pierced through the rubber jacket.

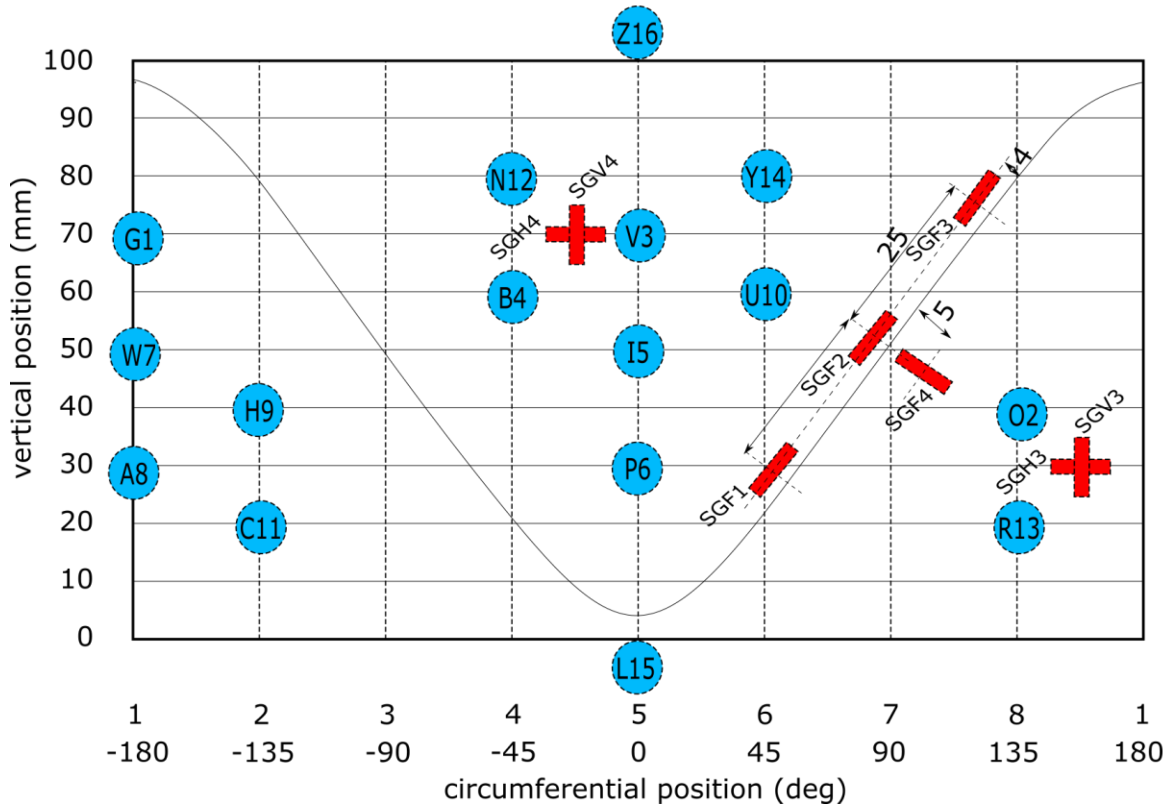

Figure S2. Sensor map with blue circles corresponding to the acoustic sensors array, and the red rectangles referring to the strain gages.

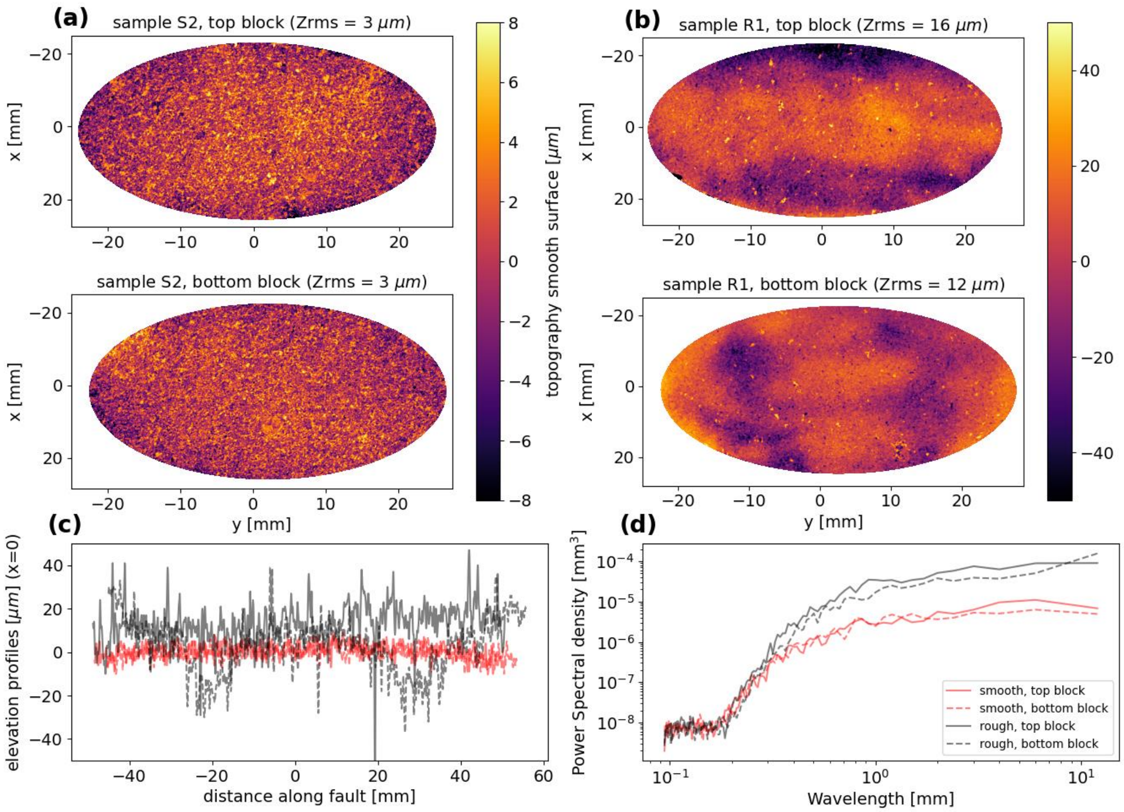

Figure S3. (a) Surface topography of top and bottom blocks for a smooth fault, sample S2. (b) Surface topography of top and bottom blocks for a rough fault, sample R1. (c) Elevation profiles along the fault surfaces major axis (at x=0) for the rough and smooth faults, top and bottom blocks. (d) Spectral analysis of the elevation profiles.

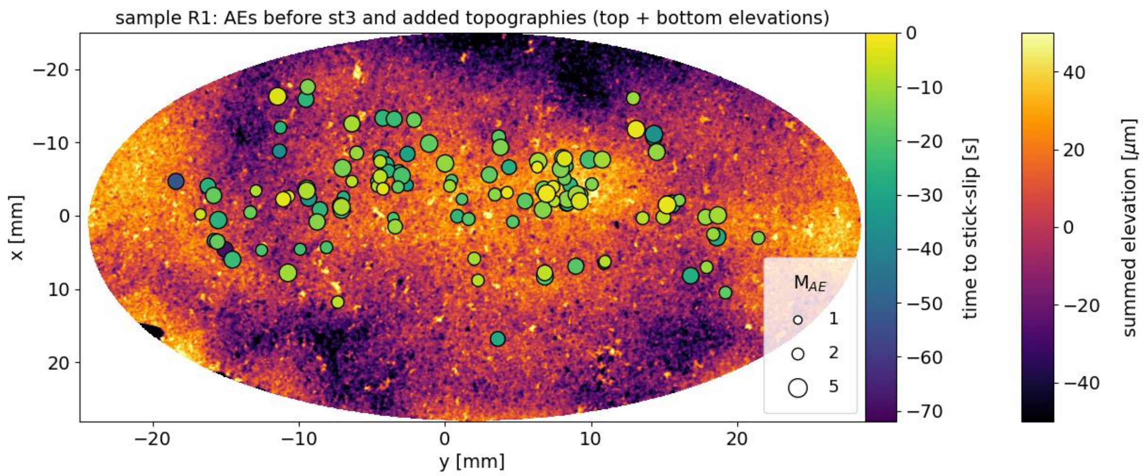

Figure S4. Added topographies of the rough surfaces from sample R1 (top block topography + bottom block topography) with superimposed acoustic emissions before stick-slip event st3.

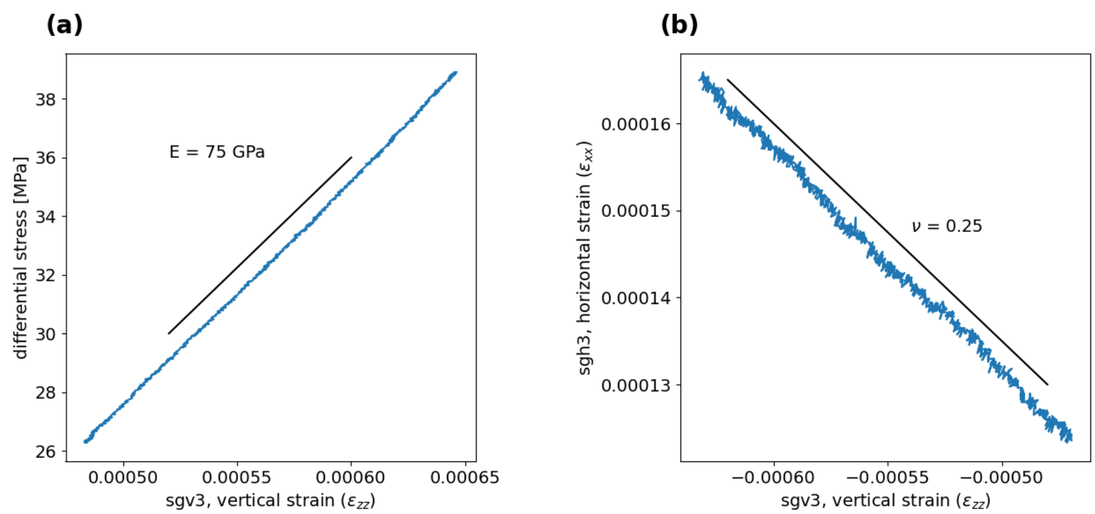

Figure S5. Elastic parameters estimates for La Peyratte granite samples, during elastic loading: (a) Young's modulus and (b) Poisson's ratio.

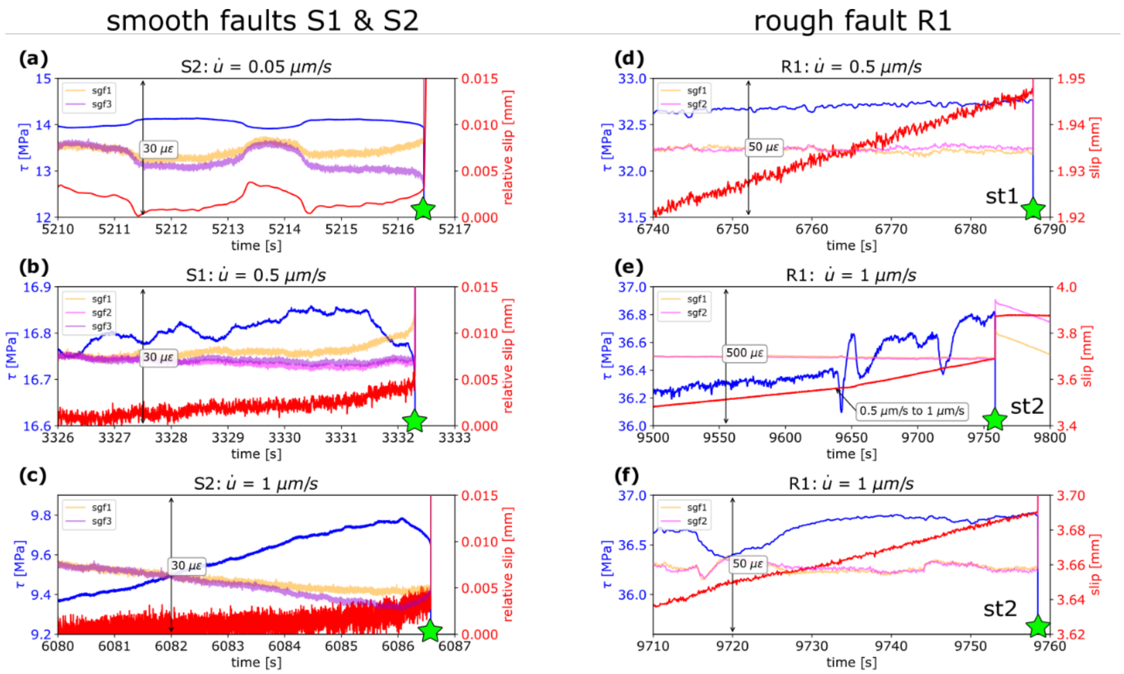

Figure S6. Evolution of shear stress (blue curve), slip (red curve) and available fault parallel strain gage signals (purple, pink and yellow curves), during a few seconds prior to stick-slip events for the smooth faults (a, b & c), and during a few tens of seconds prior to stick-slips events for the rough fault (d, e & f). The green stars indicate the stick-slips onsets. The change of load point displacement rate, from 0.5 µm/s to 1 µm/s prior to st2, is indicated on subplot (e).

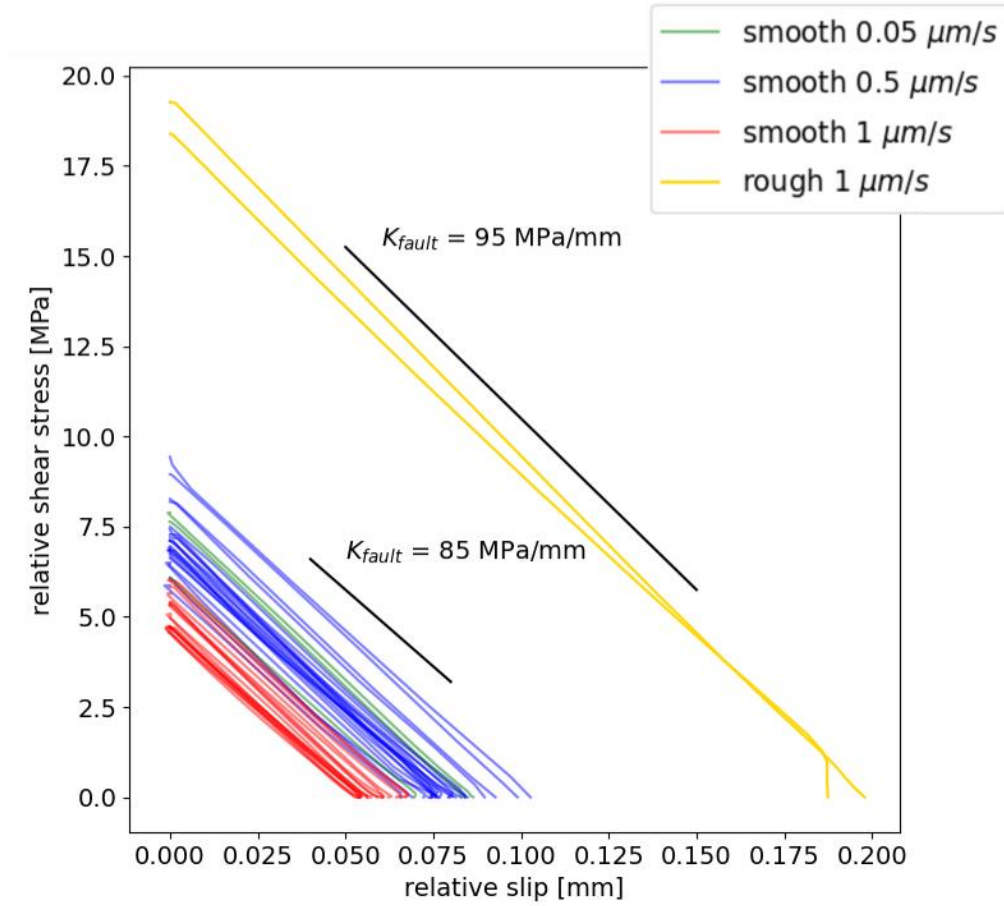

Figure S7. Shear stress versus fault slip (offset values), during stick-slip events for the smooth faults and the rough fault. The slopes corresponding to fault stiffness are indicated with solid black lines. The average fault stiffness K_{fault} is measured to be about $K_{\text{fault}} \approx 90$ MPa/mm. In addition, the axial stiffness of loading system K_{system} is estimated to be about $K_{\text{system}} = 1/(1/K_{\text{sample}} + 1/K_{\text{machine}}) = 229$ MPa/mm, where $K_{\text{sample}} = E / L = 750$ MPa/mm is the elastic stiffness of the sample with E and L being Young's modulus and sample length, respectively, and $K_{\text{machine}} = 330$ MPa/mm is the axial stiffness of loading machine. If we project fault slip and shear stress along the cylinder axis (z axis), along which loading forces are applied, we obtain a correcting factor c (i.e., $c = 1/(\sin\theta\times\cos^2\theta) = 2.66$, see equations (1) and (2)) for the equivalent axial stiffness of the fault. This results in the equivalent axial stiffness of the faults between 226 and 252 MPa/mm, comparable to axial stiffness of loading system.

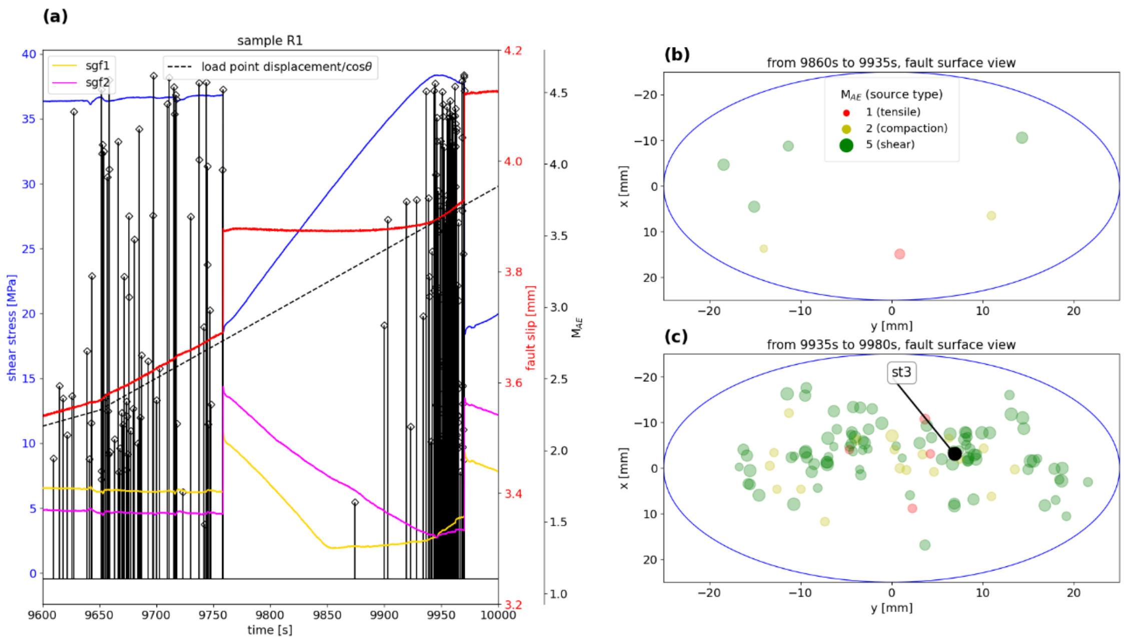

Figure S8. (a) Evolution of shear stress, slip, AEs and strain signals prior to stick-slip events st2 and st3 for sample R1. The load point displacement is indicated at a dashed black line. Loading point velocity was manually increased from 0.5 µm/s to 1 µm/s at *t* = 9650 s. (b) Locations of AE events occurring in the time window between t=9860 s and t=9935 s during which local slip occurs only close to strain gage sgf1 (sgf1 is relaxing and sgf2 remains in compression). (c) Locations of AE events occurring in the time window between t=9935 s to t=9980 s that corresponds to the onset of relaxation for sgf2, until the emergence of stick-slip event st3.

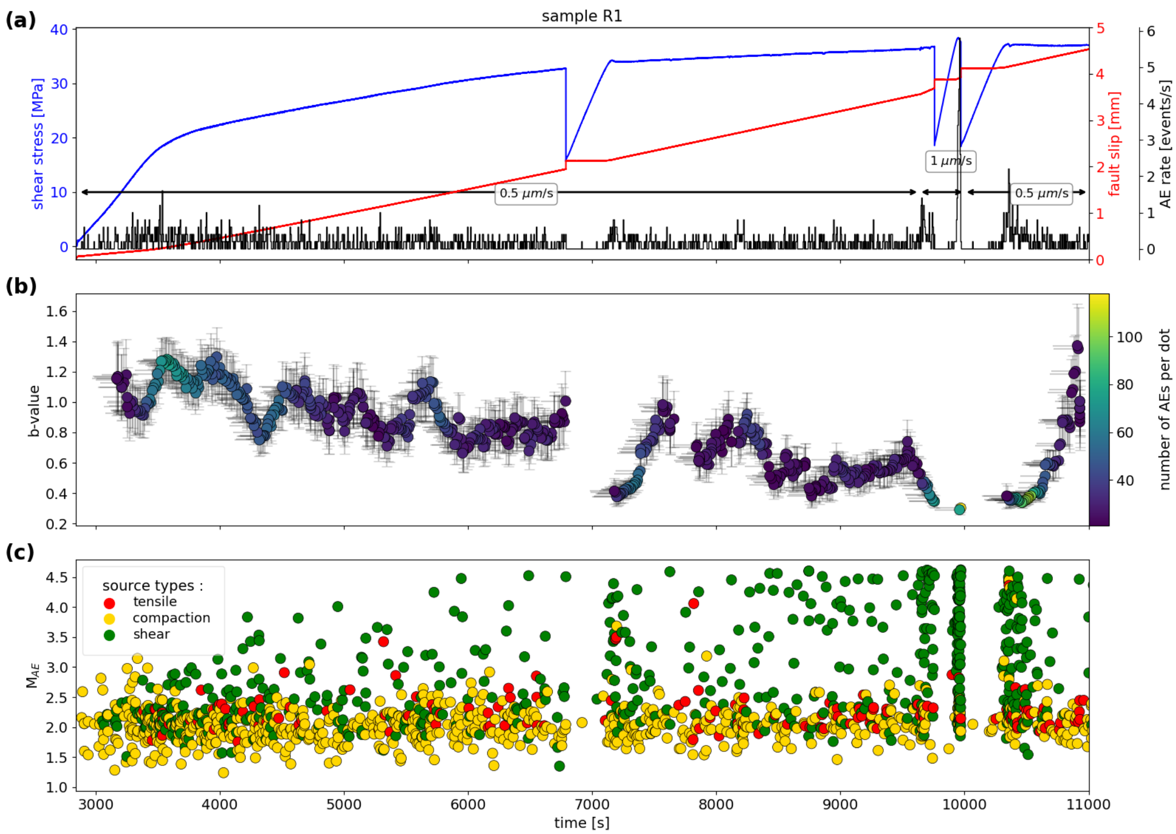

Figure S9. a) Evolution of shear stress, slip and AE rate for the rough sample R1. b) Evolution of *b*-value from AEs recorded on sample R1. The time windows for *b*-values calculations are indicated by horizontal grey lines, and the number of events during a time window is indicated on the color scale. Uncertainties are reported as vertical grey lines. c) Evolution of AE amplitude and type

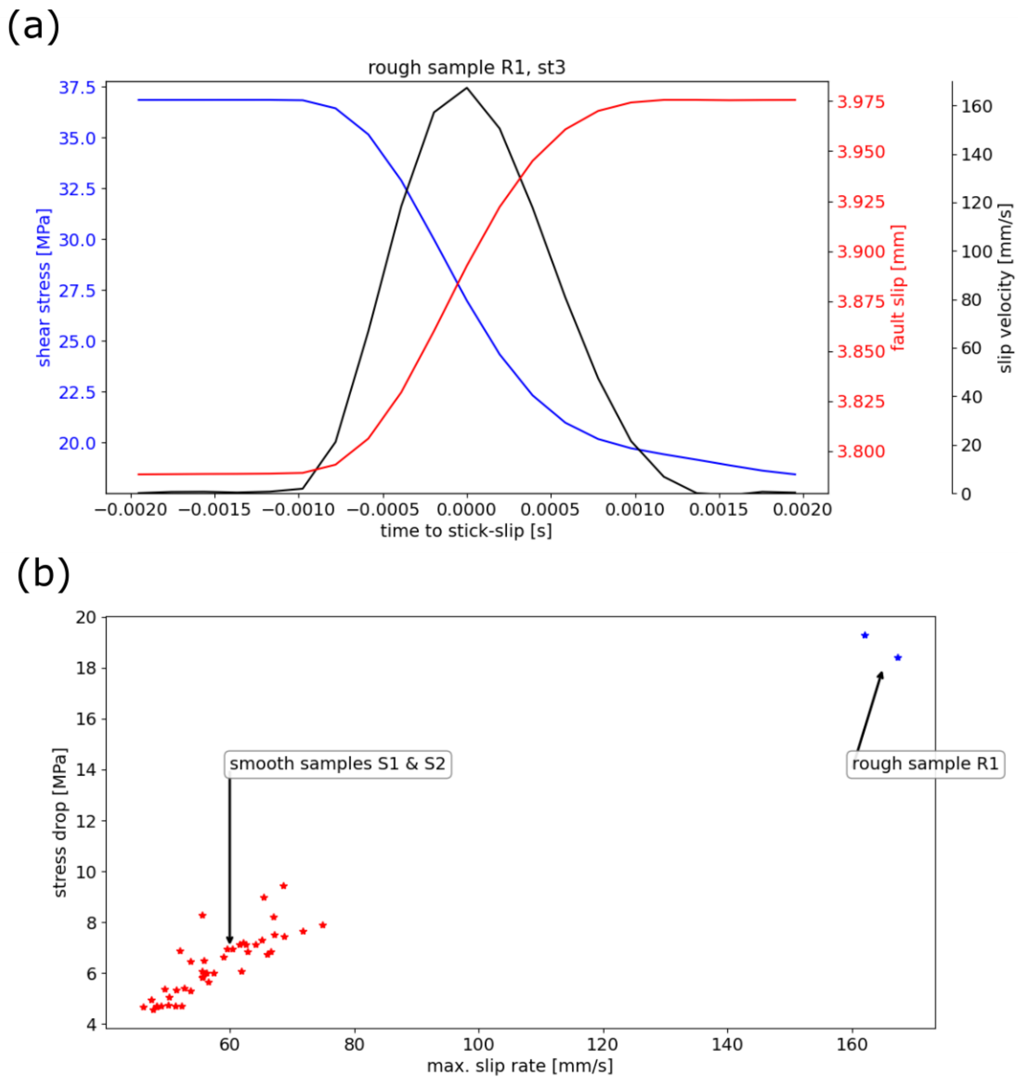

Figure S10. (a) Evolution of shear stress, slip and slip velocity during stick-slip event st3 on the rough fault R1. (b) Stress drop vs. maximum slip velocities during stick-slip events on smooth and rough faults.

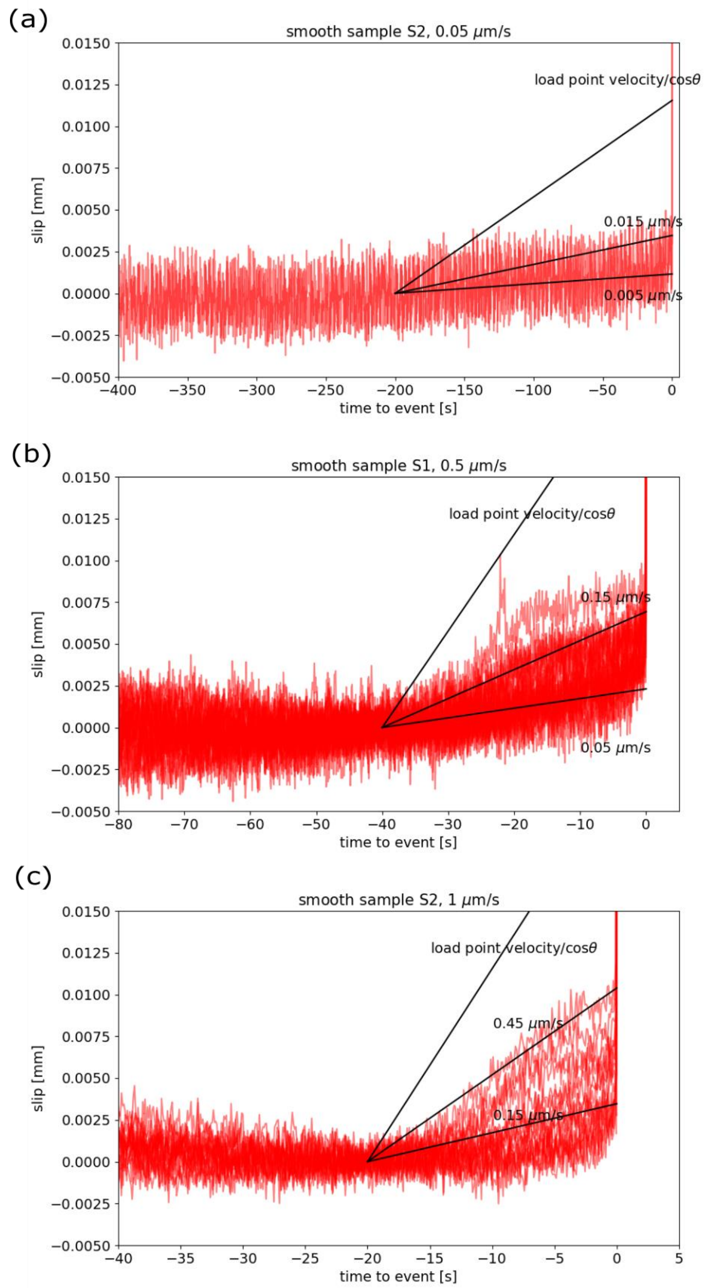

Figure S11. Preparatory slip prior to stick-slip events on smooth faults, and comparison with the load point velocities at (a) 0.05 μm/s with slip offset to zero 200 s before the events, (b) 0.5 μm/s with slip offset to zero 40 s before the events, and (c) 1 μm/s with slip offset to zero 20 s before the events.